Philosophical Magazine

ISSN: 1478-6435 (Print) 1478-6443 (Online) Journal homepage: http://www.tandfonline.com/loi/tphm20

The under-pressure behaviour of mechanical, electronic and optical properties of calcium titanate and its ground state thermoelectric response

N. A. Noor, S. M. Alay-e-Abbas, M. Hassan, I. Mahmood, Z. A. Alahmed & A. H. Reshak

To cite this article: N. A. Noor, S. M. Alay-e-Abbas, M. Hassan, I. Mahmood, Z. A. Alahmed & A. H. Reshak (2017) The under-pressure behaviour of mechanical, electronic and optical properties of calcium titanate and its ground state thermoelectric response, Philosophical Magazine, 97:22, 1884-1901, DOI: 10.1080/14786435.2017.1320440

To link to this article: http://dx.doi.org/10.1080/14786435.2017.1320440

Published online: 28 Apr 2017.

PHILOSOPHICAL MAGAZINE, 2017
VOL. 97, NO. 22, 1884–1901
https://doi.org/10.1080/14786435.2017.1320440

Taylor & Francis
Taylor & Francis Group

The under-pressure behaviour of mechanical, electronic and optical properties of calcium titanate and its ground state thermoelectric response

N. A. Noor[a], S. M. Alay-e-Abbas[b,c], M. Hassan[d], I. Mahmood[a], Z. A. Alahmed[e] and A. H. Reshak[f,g]

[a]Centre for High Energy Physics, University of the Punjab, Lahore, Pakistan; [b]Department of Physics, Government College University Faisalabad, Faisalabad, Pakistan; [c]Department of Physics, University of Sargodha, Sargodha, Pakistan; [d]Department of Physics, University of the Punjab, Lahore, Pakistan; [e]Department of Physics and Astronomy, College of Science, King Saud University, Riyadh Saudi Arabia; [f]New Technologies – Research Center, University of West Bohemia, Pilsen, Czech Republic; [g]School of Material Engineering, University Malaysia Perlis, Kangar, Malaysia

ABSTRACT

In this study, the elastic, electronic, optical and thermoelectric properties of $CaTiO_3$ perovskite oxide have been investigated using first-principles calculations. The generalised gradient approximation (GGA) has been employed for evaluating structural and elastic properties, while the modified Becke Johnson functional is used for studying the optical response of this compound. In addition to ground state physical properties, we also investigate the effects of pressure (0, 30, 60, 90 and 120 GPa) on the electronic structure of $CaTiO_3$. The application of pressure from 0 to 90 GPa shows that the indirect band gap (Γ-M) of $CaTiO_3$ increases with increasing pressure and at 120 GPa it spontaneously decreases transforming cubic $CaTiO_3$ to a direct (Γ-Γ) band gap material. The complex dielectric function and some optical parameters are also investigated under the application of pressures. All the calculated optical properties have been found to exhibit a shift to the higher energies with the increase of applied pressure suggesting potential optoelectronic device applications of $CaTiO_3$. The thermoelectric properties of $CaTiO_3$ have been computed at 0 GPa in terms of electrical conductivity, thermal conductivity and Seebeck coefficient.

ARTICLE HISTORY
Received 18 September 2016
Accepted 9 April 2017

KEYWORDS
Mechanical properties; electronic properties; optical properties; thermoelectric response

1. Introduction

The perovskite oxide of titanium in the 4+ oxidation state ($A^{2+}Ti^{4+}O^{2-}_3$) have been extensively studied owing to their high potential for practical device applications [1–6]. These compounds have also been widely explored for addressing

CONTACT A. H. Reshak maalidph@yahoo.co.uk

fundamental research issues, e.g. the kinetics of structural phase transition induced by various parameters like, temperature, pressure, strain, impurities and defects [7–9]. Ideally the $ATiO_3$ perovskites oxides adopt a cubic crystal structure where the B site cation resides at the centre of an octahedra formed by six O atoms, whereas the A site cation occupies a site which is 12-fold coordinated with the O atoms [10]. Among these materials, $CaTiO_3$ (CTO) exhibits orthorhombic, tetragonal and cubic phases, depending on the pre- and post-growth conditions, which can lead to utilising this material in devices requiring semiconductor, dielectric and catalyst properties. In addition, various experimental techniques have been employed for the growth of CTO in the form of bulk [11], thin film [12], nanocrystal [13] and super-lattices [14]. The stable cubic modification of CTO [15] can be attributed to the ionic radii of Ca since the barium containing titante of the same family ($BaTiO_3$) exhibits a stable tetragonal structure [16]. Recent experimental works suggest that the strain offered by the substrates to the CTO can affect the crystal structure which can give rise to symmetry induced ferroelectric polarisation [17].

In the past, numerous theoretical investigation have been carried out for exploring the bulk and surface properties of CTO using first-principles calculations. For instance, Wang et al. [18] used density functional theory (DFT) to explore the influence of Ti atom's displacements on ferroelectric properties of CTO. The (0 0 1) surfaces CaO and TiO_2 terminations of CTO have been investigated [19] by Wang et al., while the influence of intrinsic vacancy defects on the opto-electronic properties of CTO in both orthorhombic and cubic phases are also available in the literature [20]. Although a lot of useful electronic and optical data has been reported for the ground state properties of CTO using standard DFT approaches [21,22], a thorough investigation of the electronic structure, optical properties and the thermoelectric response of CTO with improved exchange-correlation energy functional of DFT at ground state as well as under the application of hydrostatic pressure is still lacking in literature.

In this study, we compute the ground state mechanical, electronic, optical and thermoelectric properties of cubic CTO by employing recently developed exchange-correlation functionals of DFT. Since the response of ceramic materials, such as CTO, to the application of external pressures is extremely important to determine their potential device applications, we aim at exploring the pressure dependence of elastic, electronic and optical properties of CTO. Since increasing demands of energy efficient devices has triggered a search for alternative materials, the thermoelectric energy is of prime interest as it can be useful in generating electricity from the wasted heat energy during device operation. Thermoelectric materials find wide range of applications and exist in semiconductors, semimetal and ceramics in single crystal, poly-crystal and nano-composite forms. Motivated by this, we have also explored the ground state thermoelectric properties of CTO [23–25] which have not been investigated earlier with *ab initio* calculations, to the best of our knowledge.

2. Computational method

The DFT calculations are performed using the WIEN2k code which is based on full-potential linearised augmented plane wave (FP-LAPW) method [26]. The structural parameters have been optimised using the PBEsol generalised gradient approximation (GGA) [27], while the modified Becke-Johnson [28] potential proposed by Tran and Blaha (TB-mBJ) [29] has been employed for electronic and optical properties of CTO. For the muffin-tin model of crystal potential, the plane wave cut-off in the interstitial region is controlled by setting $R_{MT} \times K_{max} = 8$, while inside the atomic spheres the maximum value angular momentum has been fixed at 10 for the wave function expansion. A 12 × 12 × 12 k-mesh in the irreducible wedge of the Brillouin zone has been used for performing self-consistent calculations which were allowed to terminate when the energy difference in two consecutive self-consistent cycles was below 10^{-4} Ry. The convergence of the calculated properties was checked by increasing $R_{MT} \times K_{max} = 9$ and the k-mesh to 20 × 20 × 20 k-mesh. Our test calculations confirmed the reliability of total energy-dependent properties computed using the all-electron FP-LAPW method [30,31]. The standard Boltzmann kinetic transport theory and its rigid band implementation available in the BoltzTrap code [32] has been employed for calculating the thermoelectric properties. Since band structure calculations are unable to determine relaxation time, the constant value of relaxation time available in the BoltzTrap code is used [32].

3. Results and discussions

3.1. Structural and elastic properties

The equilibrium volumes of the cubic cell and the bulk modulus (B_0) for CTO have been computed by fitting the Birch–Murnaghan equation of state to the computed energy vs. volume data. The calculated values are presented in Table 1, where an excellent agreement with the experimental and other theoretically values is evident. As expected, the lattice parameters of CTO show decrease with increasing pressure (Figure 1(a)) that can be used for tuning the electronic properties of CTO [33].

The elastic properties of cubic CTO have been evaluated by employing Charpin method [26]. Within the Charpin method the elastic properties of cubic crystals are elucidated by the elastic constants C_{11}, C_{12} and C_{44}. The computed values of the C_{11}, C_{12} and C_{44} are presented in Table 1 which show good agreement with previous experimental as well as theoretical reports [34,35,40]. The bulk modulus, B_0, can be computed using the calculated elastic constants given by the expression

$$B_0 = \frac{C_{11} + 2C_{12}}{3} \tag{1}$$

Our calculated value of 190.18 GPa obtained from Equation (1) is close to the value obtained from Birch–Murnaghan equation of state which confirms the

Table 1. Calculated properties of $CaTiO_3$ at 0 GPa computed using PBEsol GGA functional.

	$CaTiO_3$		
Parameter	This work	Other calculations	Experimental
a_0	3.844	3.88[a]	3.859[b]
B_0	189.203[c], 190.18[d]	174.6[e]	176[f]
E_g (Γ-M)	1.98 (GGA), 2.93 (mBJ)	1.5[g]	3.5[h]
C_{11}	370.12	331.4[e]	
C_{12}	100.20	96.2[e]	
C_{44}	105.36	95.9[e]	
ζ	0.420		
E	289.92	104.1[e]	
G	116.34		
A	0.78		
B_0/G	1.626[c], 1.635[d]		

Note: For the sake of comparison the available experimental and theoretical data is also provided. a_0: lattice parameters (Å); B_0: bulk modulus (GPa); E_g (Γ-M): the indirect fundamental energy band gap (eV); C_{11}, C_{12} and C_{44}: the elastic constants (GPa); ζ: Kleinman parameter (GPa); E: Young's modulus (GPa); G: shear modulus (GPa); A: anisotropy factor (dimensionless); B_0/G: the ratio of bulk modulus and shear modulus (dimensionless).

[a]Ref. [19].
[b]Ref. [40].
[c]From Birch–Murnaghan equation of state (FP-LAPW method).
[d]From $B_0 = \frac{C_{11}+2C_{12}}{3}$
[e]Ref. [34].
[f]Ref. [41].
[g]Ref. [42].
[h]Ref. [43].

reliability of the results presented herein. The variation of C_{11}, C_{12} and C_{44} and B_0 as a function of applied pressure is shown in Figure 1 (b) where one can easily see that all of these values increase linearly with increasing pressure. This should be expected since the increase in material's density resulting from the decrease of volume causes an increase in the values of elastic constants and bulk modulus B_0. The cubic phase of CTO is found to be mechanically stable as it obeys the mechanical stability criteria [34,35]:

$$C_{11} - C_{12} > 0 \tag{2}$$

$$C_{44} > 0 \tag{3}$$

$$C_{11} + 2C_{12} > 0 \tag{4}$$

and

$$C_{12} < B_0 < C_{11} \tag{5}$$

To further explore the mechanical behaviour of CTO, we have computed the Kleinman parameter, ζ (GPa), anisotropy factor, A, Young's modulus, E (GPa), shear modulus, G (GPa) and the ratio of bulk modulus and shear modulus B_0/G using the calculated C_{11}, C_{12} and C_{44} listed in Table 1. The Kleinman parameter describes the ratio of the possibility of bond bending (which is minimum for a value close to zero) to that of the bond stretching. Our calculated value of Kleinman parameter 0.420 (see Table 1) indicates that at ground state bond bending is less favored. Even at 120 GPa, the calculated value of Kleinman parameter

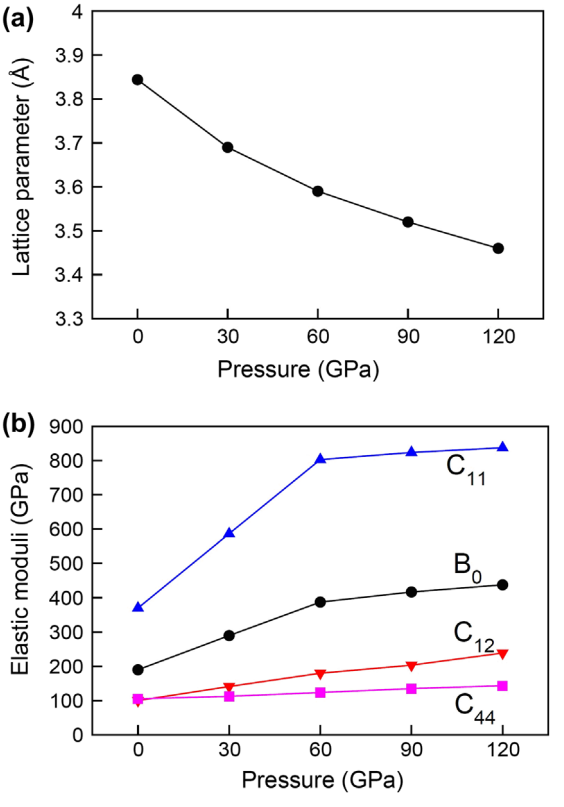

Figure 1. (colour online) (a) The calculated lattice parameters and (b) the elastic constants C_{11}, C_{12}, C_{44} and bulk modulus B_0 for $CaTiO_3$ plotted as a function applied pressures (0–120 GPa).
Note: All results computed using PBEsol GGA functional.

is 0.401, suggesting that even under the application of high pressure the bond bending is minimum in CTO [7].

The calculated value of anisotropy factor A is found to be 0.78. This shows that CTO is mechanically anisotropic since the values of A deviates from unity which represents a mechanically isotropic material. We also present the calculated Young's Modulus (E) in Table 1 which defines the tensile elasticity of a material. In order to identify the ductile or brittle nature of CTO, the B_0/G is calculated by dividing Bulk modulus B_0 with shear Modulus G. The critical value of B_0/G is 1.75 below which a material demonstrates brittle nature. Our calculated values of 1.626 and 1.635 using bulk modulus computed from Birch–Murnaghan equation of state and Equation (1), respectively, predict CTO to be brittle.

3.2. Electronic properties

Since experimental [7] as well as theoretical [8] under pressure investigations for CTO show stability of this compound at high external pressure, we have investigated the effect of hydrostatic pressure on the opto-electronic of calcium titante

by raising the pressure from 0 to 120 GPa in steps of 30 GPa. The electronic band structures of CTO calculated at five values of the applied pressures are shown in Figure 2. The band structure at 0 GPa shows that valence band maxima (VBM) and conduction band minima (CBM) are located at the M-point Γ-point, respectively. This shows that at ambient conditions CTO is an indirect band gap semiconductor. Our calculated TB-mBJ band gap, E_g, of CTO at 0 GPa is 2.930 eV which compares well with experimental E_g as compared to GGA values reported in the literature [36]. This is due to the use of TB-mBJ potential, which performs better than standard LDA and GGA functionals for reproducing the electronic properties of wide band gap materials. In addition, the valence band appears to be well confined below the Fermi level, E_F, indicating semiconducting nature of CTO which is in accordance with the previous reports [36].

The increase in pressure (from 30 to 120 GPa) appears to cause a shift in the conduction band levels towards higher energies; however, the CBM always resides at the Γ-point. On the other hand, application of pressure tends to widen the valence band of CTO with an almost linear extension in the lower part of the

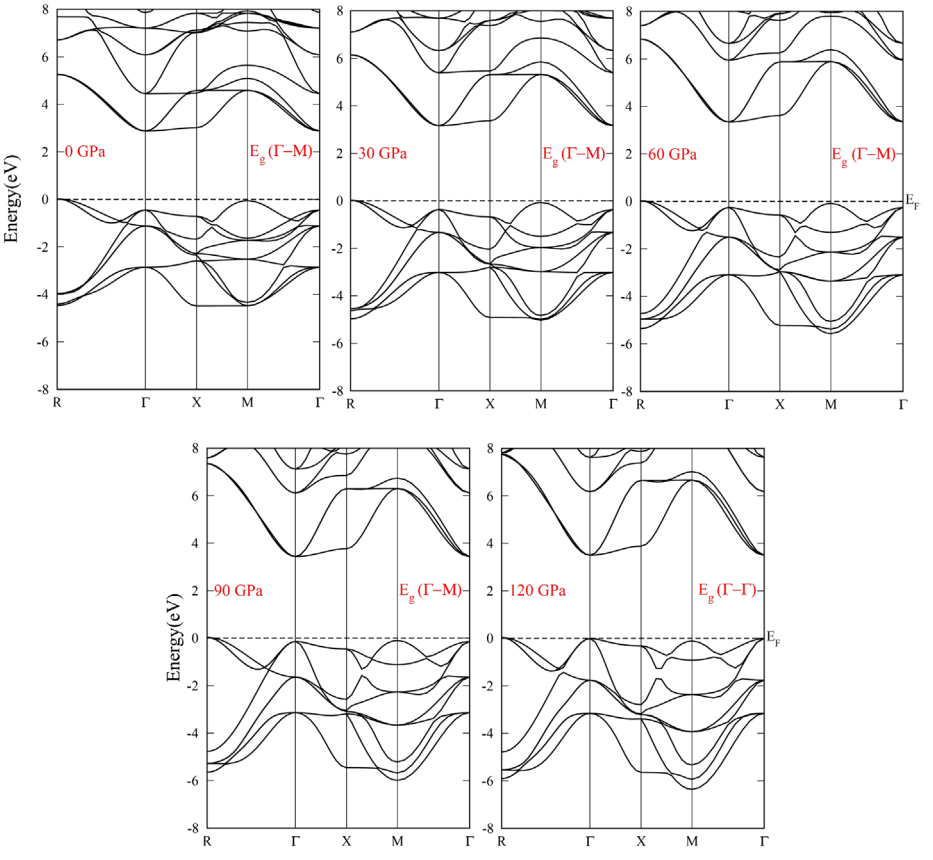

Figure 2. (colour online) The electronic band structures of $CaTiO_3$ under the application of hydrostatic pressure (0, 30, 60, 90 and 120 GPa) calculated using TB-mBJ potential.

upper valence band as the pressure increases. A relatively slow pressure induced shift in the upper part of the valence band is also evident from Figure 2 where the filled electron levels appear to shift towards higher and lower energy level at Γ-point and M-point, respectively. By comparing the behaviour of electron energy levels at these two symmetry points, it is interesting to note that the VBM resides at M-point up to 90 GPa, while the VBM is located at the Γ-point for 120 GPa indicating a transition from indirect band gap E_g (Γ-M) to direct band gap E_g (Γ-Γ). In order to further elucidate the effects observed in the electronic band structures, the total density of state (TDOS) and partial density of states (PDOS) for 4s-orbitals of Ca, 3d-orbitals of Ti and 2p-orbitals of O are plotted against energy in Figure 3. The main contribution in the hybridisation process is from the Ti-3d states and O-2p states with a minor contribution coming from the Ca-4s states. It is clear that the VBM is slightly shifted due to increase in pressure from 0 GPa to 120 GPa, while the bottom of valence band is considerably shifted towards more negative energies. Similarly, appreciable shift of the states in the conduction band toward higher energy can be observed, which leads to increase

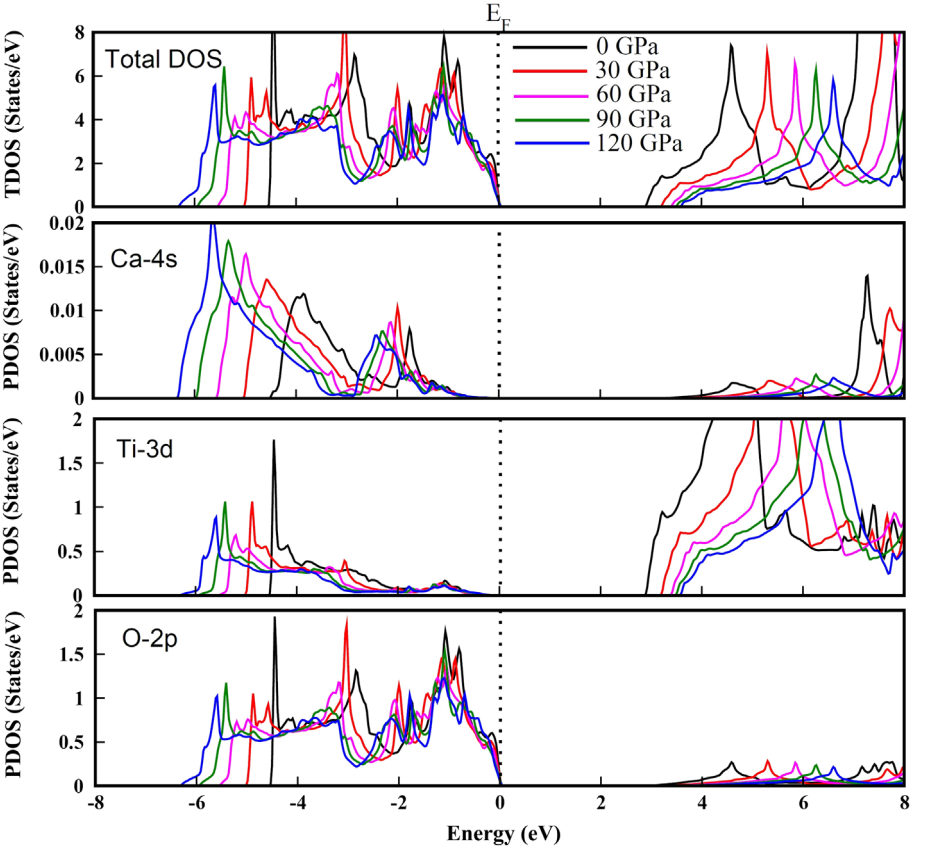

Figure 3. (colour online) The total and partial density of states for $CaTiO_3$ at 0, 30, 60, 90 and 120 GPa calculated using TB-mBJ potential.

of the band gap. Comparison of Figures 2 and 3 suggests that the hybridisation of Ti-3d and O-2p state is modified with the increasing pressure. At 120 GPa the contribution of the O-2p states to the upper part of the valence band decreases considerably which causes the occupied O-2p states at the VBM to rise towards the E_F at the Γ-point and consequently transformers indirect band gap CTO to a direct band gap material.

The calculated energy band gaps and the absolute energy separation of the core level (not shown in Figure 2) from the valence band edge (VBE) and conduction band edge (CBE) at Γ and M symmetry points are shown in Figure 4. The calculated energy band gaps (E_g(Γ-Γ), E_g(M-M) and E_g(Γ-M)) clearly show an indirect to direct band gap transformation in cubic CTO at 120 GPa. The crossover of the E_g(Γ-Γ) and E_g(Γ-M) lines in Figure 4(a) allows us to predict that cubic CTO adopts a direct fundamental energy band gap for pressure >100 GPa. The transformation of indirect band gap to direct band gap can be justified by the fact that the decrease/increase in the lattice volume/pressure results in increased hybridisation. As a consequence, an enhancement in the repulsion occurs in the crystal field causing an increase in band gap which is dictated by the shift of CBM to higher energies. The energy separation between core level and the CBE at Γ and M symmetry points in Figure 4(c) clearly shows that the conduction band moves almost linearly away from the E_F with increasing pressure. On the other hand, the difference of energy between the core level and VBE at Γ and M symmetry points show increasing and decreasing separation, respectively, as pressure increases from 0 GPa to 120 GPa. Consequently, the VBM shifts from the M-point to the Γ-point at a pressure of 120 GPa.

3.3. Optical properties

The exposure of a material to incident radiations may result in the absorption of incident energy (photon) by an electron in valence band which gets excited to the conduction band states. Since the possibility of the absorption of a photon depends strongly on the available electrons energy levels, optical properties are directly related with the electronic band structure of a material. In this regard, the computation of the complex dielectric function ($\varepsilon(\omega) = \varepsilon_1(\omega) + \varepsilon_2(\omega)$) provides useful information concerning the optical response of a material. The selection rule for allowed optical transition in a material is governed by the momentum matrix element which is related to the imaginary part of complex dielectric function ($\varepsilon_2(\omega)$) by

$$\varepsilon_2(\omega) = \frac{e^2\hbar}{\pi m^2\omega^2}\sum_{v,c}\int_{BZ}\left[|M_{cv}(k)|^2\delta[\omega_{cv}(k)-\omega]\right]d^3k \tag{6}$$

In above equation, $M_{cv}(k) = \langle u_{ck}|\delta e|u_{vk}\rangle$ and δ are momentum dipole elements, and potential vector, respectively, while e, M and ω represent the charge, mass

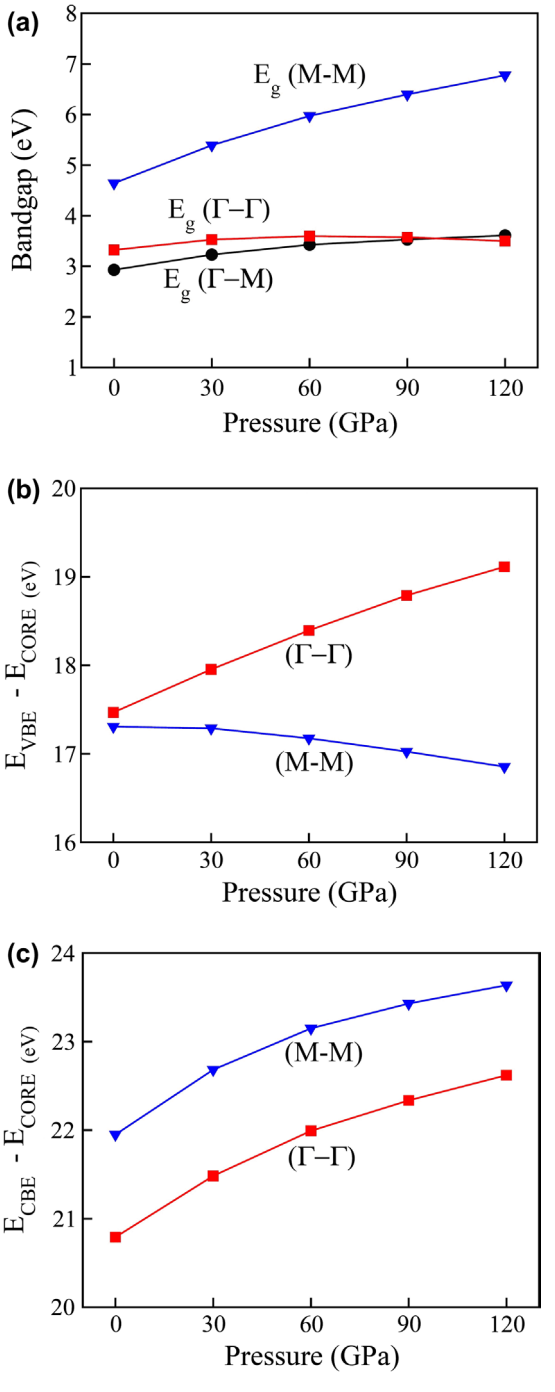

Figure 4. (colour online) Pressure induced variation in (a) direct and indirect band gaps at selected symmetry points ((Γ-Γ), (Γ-M) and (M-M)). The absolute energy separation of the core level (not shown in Figure 2) from the (b) VBE and (c) CBE at Γ and M symmetry points as a function of applied pressure.

Note: All results obtained using TB-mBJ potential.

and angular frequency associated with electrons. $M_{cv}(k)$ represents the matrix elements for direct transitions between valance band state $|u_{vk}\rangle$ and conduction band states $|u_{ck}\rangle$ such that the transition energy is equal to $E_{ck} - E_{vk}$. The real part of the complex dielectric function, on the other hand, is calculated by employing the Kramers–Krönig relation [37],

$$\varepsilon_1(\omega) = 1 + \frac{2}{\pi} P \int_0^{\infty} \frac{\omega' \varepsilon_2(\omega')}{\omega'^2 - \omega^2} d\omega' \tag{7}$$

The calculated values of real and imaginary parts of the complex dielectric function for various values of the applied external pressure are plotted in Figure 5 against incident photon's energy ranging from 0 to 30 eV. It is evident that the major peaks of $\varepsilon_1(\omega)$ for CTO are shifted to higher energy values with increasing external pressure. Therefore, the transparency of CTO to incident electromagnetic radiations of lower energies increases with the application of pressure. Further increase in the incident photon's energy results in the decrease of $\varepsilon_1(\omega)$ which finds a minimum beyond 5 eV. The real part of the complex dielectric function for 0 GPa reveals as minima between 5 and 6 eV and shows a second maxima just

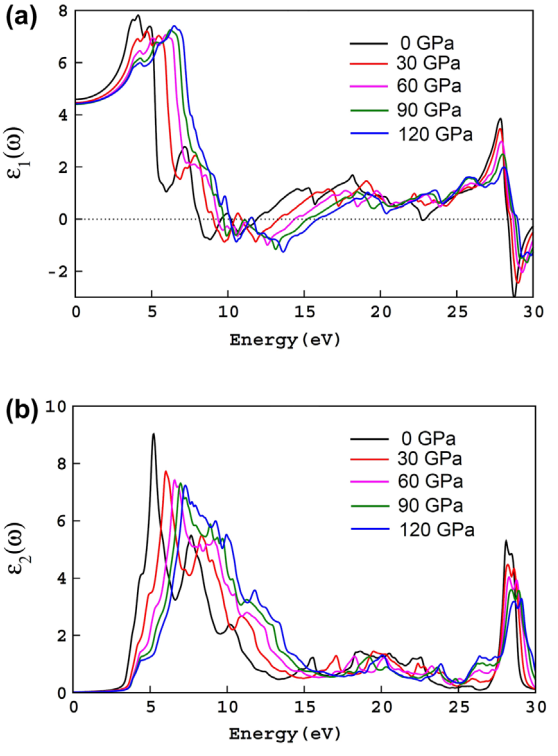

Figure 5. (colour online) The (a) Real $\varepsilon_1(\omega)$, and (b) imaginary, $\varepsilon_2(\omega)$, parts of the dielectric function plotted against incident photon's energy at various applied pressures (0–120 GPa) calculated using TB-mBJ potential.

below 7.5 eV. This second maxima of $\varepsilon_1(\omega)$ tends to disappear with the increase of pressure from 0 to 120 GPa. Beyond 7.5 eV, all the $\varepsilon_1(\omega)$ curves show a shift from positive values to negative values. The negative values of $\varepsilon_1(\omega)$ demonstrate that between 7.5 and 15 eV CTO attenuates incident electromagnetic waves. The onset of this attenuation is clearly shifted to higher energy values as the pressure is increased from 0 to 120 GPa. Between 15 and 28 eV, $\varepsilon_1(\omega)$ retains positive values. The systematic shift of the $\varepsilon_1(\omega)$ towards higher energy values of incident photon's energy reveals that hydrostatic pressure can be utilised for tuning the optical response of CTO.

The static dielectric constant ($\varepsilon_1(0)$) is obtained from the zero frequency limit of incident phtoton's energy which is plotted as a function of pressure in Figure 6. It is clear that $\varepsilon_1(0)$ decreases from 4.592 to 4.404 when the pressure is increased from 0 GPa to 90 GPa, while a value of 4.433 is obtained for 120 GPa. These results are in accordance with the variation of the energy band gaps shown in Figure 4(a) where a transition from indirect (M-Γ) to direct (Γ-Γ) band gap results in lower fundamental energy band gap at 120 GPa. The inverse behaviour of $\varepsilon_1(0)$ satisfies the Penn's model [38], $\varepsilon_1(\omega) \approx 1 + (\hbar\omega/E_g)$ where ω_p is the plasma frequency.

The refractive index $n(\omega)$, extinction co-efficient $k(\omega)$, reflectivity $R(\omega)$, optical conductivity $\sigma(\omega)$and absorption coefficient $\alpha(\omega)$ are computed from the calculated $\varepsilon_1(\omega)$ and $\varepsilon_2(\omega)$ using [39]

$$n^2 - k^2 = \varepsilon_1 \tag{8}$$

$$2nk = \varepsilon_2 \tag{9}$$

$$R = \frac{(n-1)^2 + k^2}{(n+1)^2 + k^2} \tag{10}$$

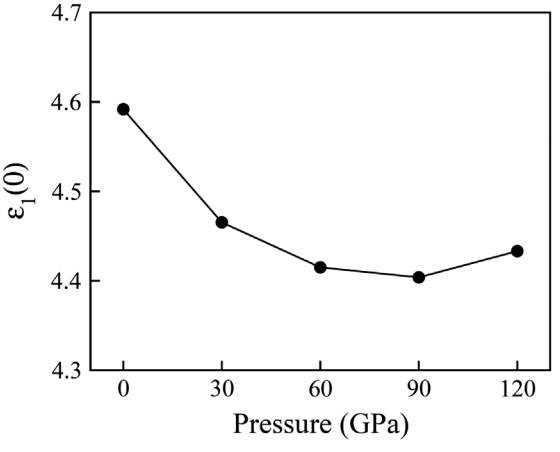

Figure 6. The static part of the dielectric function, $\varepsilon_1(0)$, illustrating variation with increasing pressure calculated using TB-mBJ potential.

$$\sigma(\omega) = \frac{4\pi k(\omega)}{\lambda} \tag{11}$$

The refractive index, $n(\omega)$, and the extinction coefficient, $k(\omega)$, of CTO are plotted in Figure 7(a–b). It is clear that the variation of $n(\omega)$ (which governs the ability of CTO to allow the electromagnetic radiations to pass through it) and $k(\omega)$ (which dictates CTO's capability to attenuate electromagnetic radiations) with photon's energy is closely related to the variation of $\varepsilon_1(\omega)$ and $\varepsilon_2(\omega)$, respectively, presented in Figure 5. From the calculated variation of reflectivity $R(\omega)$ with the incident photon's energy shown in Figure 8(a) it is clear that reflectivity is maximum wherever $\varepsilon_1(\omega)$ adopts minimum or a negative value. The first maxima in $R(\omega)$ arises around 5 eV and the second and third maximas are located between 7.5 and 15 eV. All the calculated curves of $R(\omega)$ are shifted towards higher energy values as the external pressure is increased showing that reflectivity of cubic CTO can be tuned with the application of pressure.

The variation of absorption coefficient, $\alpha(\omega)$, is presented in Figure 8(b) for different values of applied pressures (0–120 GPa) as a function of incident photon's energy. In all cases, $\alpha(\omega)$ is zero for the incident energy values which are less than the fundamental energy band gap values shown in Figure 4(a). Since the

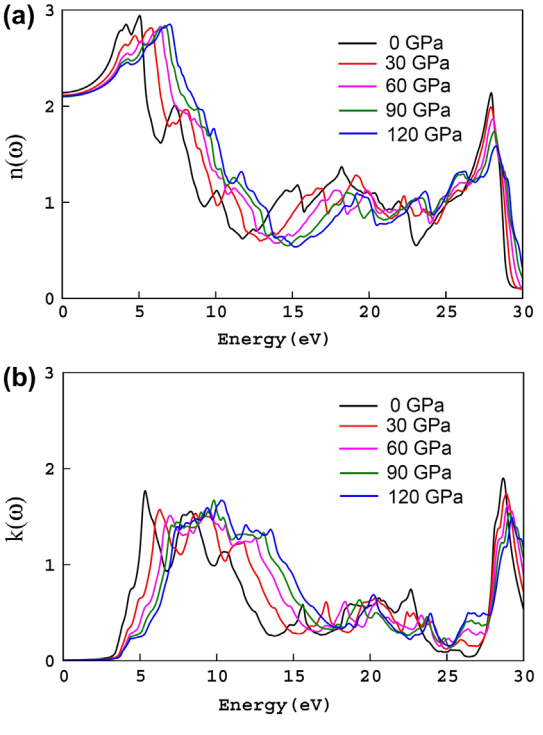

Figure 7. (colour online) The (a) Refractive index $n(\omega)$, and (b) extinction coefficient, k(ω), plotted against incident photon's energy at various applied pressures (0–120 GPa).
Note: Results obtained using TB-mBJ potential.

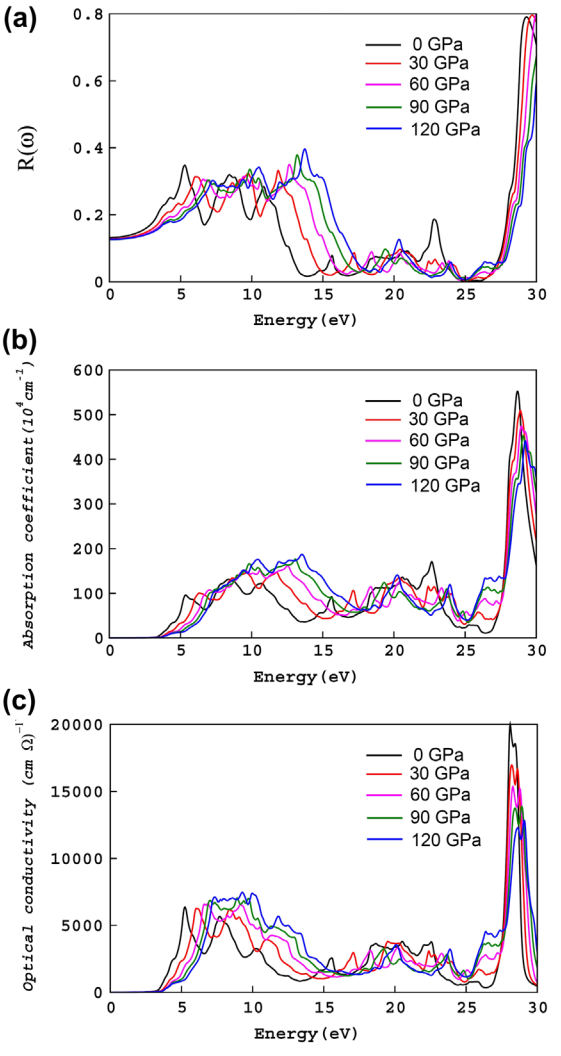

Figure 8. (colour online) The (a) Reflectivity, $R(\omega)$, (b) absorption coefficient, $\alpha(\omega)$, and (b) optical conductivity, $\sigma(\omega)$, plotted against incident photon's energy at various applied pressures (0–120 GPa).
Note: Results obtained using TB-mBJ potential.

absorption edge initially lies just below 3 eV, CTO is transparent to infrared part of the electromagnetic spectrum. On increasing the external pressure the absorption edge crosses 3 eV indicating a shift to the ultraviolet part of the electromagnetic spectrum. The plots of $\alpha(\omega)$, calculated from 0 GPa to 90 GPa shows that few peaks appear before reaching maximum absorption, which is due to the existence of indirect band gap. Interestingly, at 120 GPa indicates an approximately linear absorption with incident energy confirming the direct band gap nature of CTO at this pressure. Moreover, the absorption edge is placed below the absorption edges at 90 and 60 GPa, in confirmation with fundamental band gaps shown in Figure

4(a). Strong absorption also appears just below 30 eV; however the application of external pressure suppresses the magnitude of absorption which leads to lowest absorption at 120 GPa at high energy ranges of incident photons. The calculated optical conductivity (Figure 8(c)), $\sigma(\omega)$, depicts the conduction induced by the electrons which move from valence band to the conduction band upon absorption of incident light. Since the optical conductivity appears as a result of absorption, the features of the curves in Figure 8(b) and (c) are closely related. The peaks in Figure 8(b) and (c) represent optically induced electronic transitions between different states of the occupied valence band and the unoccupied conduction band

3.4. Thermoelectric properties

In the present study, we explore the thermoelectric behaviour of CTO at ambient pressure because CTO band gap shows an increase with the applied pressure but thermoelectric properties are mostly suitable in small band gap materials. Thermoelectricity is realised due to the heat energy, which produces potential difference across the edges of the material and is known as the Seebeck effect. The thermoelectric efficiency of a material can be evaluated at a certain value of temperature T by computing power factor which is given by σS^2. Here σ and S represent the electrical conductivity and Seebeck coefficient, respectively. The calculated electrical conductivity per relaxation time of cubic CTO at 0 GPa is plotted against temperature in Figure 9(a). The increase in temperature causes a linear increase in electrical conductivity, which is due to the thermal excitation of the electrons in the valence band. The calculated electrical conductivity is found to be 0.835×10^{19} $(\Omega\ \mathrm{m\ s})^{-1}$ at room temperature, RT (300 K), which increases to 2.224×10^{19} $(\Omega\ \mathrm{m\ s})^{-1}$ at 800 K. It is important to point out here that the calculated values of σ/τ (where τ is the relaxation time) are directly related to the band structure of cubic CTO (Figure 2) and the concentration and type of charge carriers. The electronic part of the thermal conductivity, k_e, has also been calculated for CTO and is presented in Figure 9(b). The thermal conductivity, k_e, exhibit smaller values in the low temperature range; however, it reaches to 1.413×10^{14} (W/m K s) at RT and attains maximum value of 10.547×10^{14} (W/m K s) at 800 K. Since the total thermal conductivity demonstrates material's capability for heat conduction, which depends on both the electronic and lattice contributions, the temperature dependent enhancement in k_e, (Figure 9(b)) may impede pristine CTO's potential thermoelectric device applications. However, tuning the thermal conductivity of CTO by means of chemical or mechanical strain may lead to performance suitable for practical purposes.

The Seebeck coefficient or the thermoelectric power, S, for CTO is plotted in Figure 9(c), which shows the generation of potential difference due to the temperature difference. It is clear that S increases rapidly with the rise of temperature up to 200 K and then varies relatively slowly for higher values of T. In the temperature range 450–800 K, the average value of S is found to be 205 (μV/K).

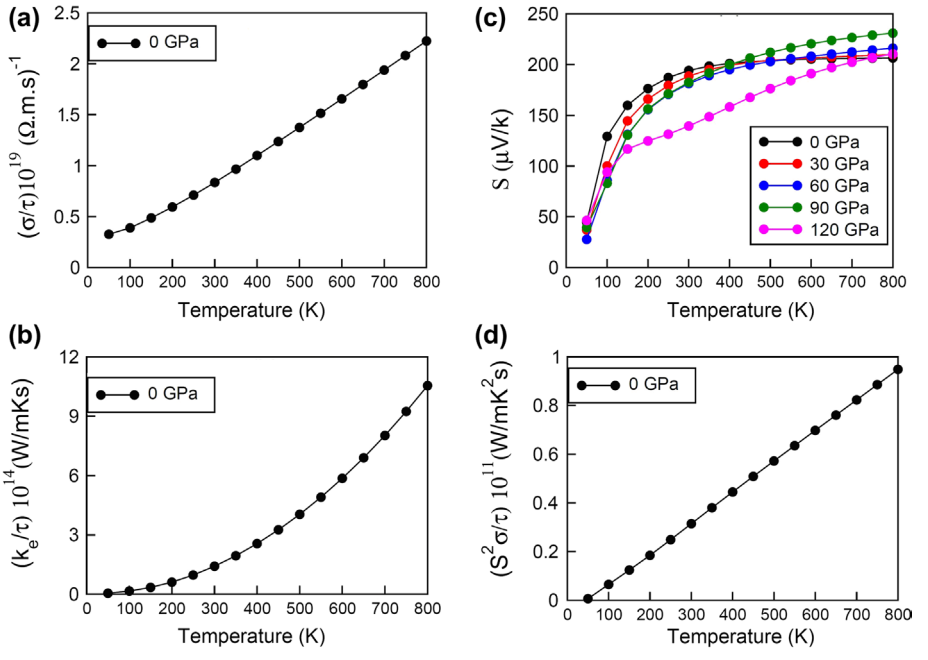

Figure 9. (colour online) The calculated (a) electrical conductivity per relaxation time, (b) thermal conductivity per relaxation time, (c) Seebeck coefficient, *S* and (d) power factor per relaxation time, as a function of temperature.
Note: All the properties, except the Seebeck coefficient, are computed only at the ground state lattice parameter (i.e. 0 GPa).

Although τ for CTO under the application cannot be estimated, we also compute the variation of *S* for CTO under the application of hydrostatic pressures. It is clear from Figure 9(c) that pressure up to 90 GPa does not cause large variation in the overall variation of S; however, at 120 GPa a considerable decrease in the Seebeck coefficient is evident for temperature ranging between 150 and 700 K. This is a direct consequence of the direct to indirect band gap transition discussed above and the resulting smaller fundamental energy band gap. The calculated power factor of CTO at 0 GPa is plotted in Figure 9(d). The linear increase of the power factor to 9.49×10^{10} W/m K^2 s at 800 K shows that CTO-based devices may be useful for higher temperatures applications. These results reveal that CTO promises potential thermoelectric device applications.

4. Conclusions

In conclusion, we have investigated the structural, elastic, electronic, optical and thermoelectric properties of cubic $CaTiO_3$ perovskite oxide using DFT. The structural and elastic properties are found to be in good agreement with the experimental data, while the TB-mBJ functional gives accurate account of electronic properties at ground state as well as under the application of hydrostatic pressure (30, 60, 90 and 120 GPa). The calculated elastic parameters for

CTO, in the cubic phase, prefers bond stretching and mechanical anisotropic is present. We also conclude that CTO has a brittle nature. Under the application of pressure, the electronic band structure of CTO shows an indirect band gap (Γ-M) up to 90 GPa, while a shift from indirect to direct band gap (Γ-Γ) is achieved at 120 GPa. It is found that the hybridisation of Ti-3d and O-2p state is enhanced with the increasing pressure that results in the appearance of direct band gap. This transformation from indirect to direct band gap indicates potential application of CTO in opto-electronic devices. The imaginary part of the dielectric function, $\varepsilon_2(\omega)$, extinction, $k(\omega)$ and absorption coefficient, $\alpha(\omega)$, indicate that CTO can absorb radiations for a wide region of electromagnetic spectra. The static part of the dielectric constant $\varepsilon_1(0)$ and the band gap show inverse relation which is in agreement with the Penn's model. The calculated thermoelectric behaviour of CTO shows that utilisation of this material in thermoelectric devices requires optimisation of thermal conductivity value. Using the values of calculated electrical conductivity, thermal conductivity and the power factor in $ZT = \frac{\sigma S^2}{k} T$, we find that CTO can achieved an efficiency of 0.075.

Disclosure statement

No potential conflict of interest was reported by the authors.

Funding

The result was developed within the CENTEM project, reg. no. CZ.1.05/2.1.00/03.0088, co-funded by the ERDF as part of the Ministry of Education, Youth and Sports OP RDI program and, in the follow-up sustainability stage, supported through CENTEM PLUS (LO1402) by financial means from the Ministry of Education, Youth and Sports under the National Sustainability Program I. This work is supported by the International Scientific Partnership Program ISPP at King Saud University [grant number ISPP# 0016]. Computational resources were provided by MetaCentrum (LM2010005) and CERIT-SC (CZ.1.05/3.2.00/08.0144) infrastructures.

References

[1] M.A. Peña and J.L.G. Fierro, *Chemical structures and performance of perovskite oxides*, Chem. Rev. 101 (2001), pp. 1981–2018.
[2] T. Lee and I.A. Aksay, *Hierarchical structure–ferroelectricity relationships of barium titanate particles*, Cryst. Growth Des. 1 (2001), pp. 401–419.
[3] M. McQuarrie, *Structural behavior in the system (Ba, Ca, Sr)TiO_3 and its relation to certain dielectric characteristics*, J. Am. Ceram. Soc. 38 (1955), pp. 444–449.
[4] N. Ohtsu, K. Sato, A. Yanagawa, K. Saito, Y. Imai, T. Kohgo, A. Yokoyama, K. Asami, and T. Hanawa, *$CaTiO_3$ coating on titanium for biomaterial application – Optimum thickness and tissue response*, J. Biomed. Mater. Res. A 82A (2007), pp. 304–315.
[5] V.V. Lemanov, A.V. Sotnikov, E.P. Smirnova, M. Weihnacht, and R. Kunze, *Perovskite $CaTiO_3$ as an incipient ferroelectric*, Solid State Commun. 110 (1999), pp. 611–614.

[6] N. Setter and R. Waser, *Electroceramic materials*, Acta Mater. 48 (2000), pp. 151–178.
[7] M. Guennou, P. Bouvier, B. Krikler, J. Kreisel, R. Haumont, and G. Garbarino, *High-pressure investigation of $CaTiO_3$ up to 60 GPa using x-ray diffraction and Raman spectroscopy*, Phys. Rev. B 82 (2010), p. 134101.
[8] J.A. Souza and J.P. Rino, *A molecular dynamics study of structural and dynamical correlations of $CaTiO_3$*, Acta Mater. 59 (2011), pp. 1409–1423.
[9] Y. Ni, Z. Zhang, D. Wang, Y. Wang, and X. Ren, *The effect of point defects on ferroelastic phase transition of lanthanum-doped calcium titanate ceramics*, J. Alloys Compd. 577 (2013), pp. S468–S471.
[10] A.S. Bhalla, R. Guo, and R. Roy, *The perovskite structure – A review of its role in ceramic science and technology*, Mater. Res. Innovat. 4 (2000), pp. 3–26.
[11] G. Gralik, A.E. Thomsen, C.A. Moraes, F. Raupp-Pereira, and D. Hotza, *Processing and characterization of $CaTiO_3$ perovskite ceramics*, Process. Appl. Ceram. 8 (2014), pp. 53–57.
[12] N. Ohtsu, K. Saito, K. Asami, and T. Hanawa, *Characterization of $CaTiO_3$ thin film prepared by ion-beam assisted deposition*, Surf. Coat. Technol. 200 (2006), pp. 5455–5461.
[13] M.R. Mohammadi and D.J. Fray, *Synthesis of highly pure nanocrystalline and mesoporous $CaTiO_3$ by a particulate sol–gel route at the low temperature*, J. Sol-Gel Sci. Technol. 68 (2013), pp. 324–333.
[14] X. Wu, K.M. Rabe, and D. Vanderbilt, *Interfacial enhancement of ferroelectricity in $CaTiO_3$/$BaTiO_3$ superlattices*, Phys. Rev. B 83 (2011), p. 020104.
[15] X. Yang, J. Fu, C. Jin, J. Chen, C. Liang, M. Wu, and W. Zhou, *Formation mechanism of $CaTiO_3$ hollow crystals with different microstructures*, J. Am. Chem. Soc. 132 (2010), pp. 14279–14287.
[16] K. Suzuki and K. Kijima, *Phase transformation of $BaTiO_3$ nanoparticles synthesized by RF-plasma CVD*, J. Alloys Compd. 419 (2006), pp. 234–242.
[17] M.D. Biegalski, L. Qiao, Y. Gu, A. Mehta, Q. He, Y. Takamura, A. Borisevich, and L.Q. Chen, *Impact of symmetry on the ferroelectric properties of $CaTiO_3$ thin films*, Appl. Phys. Lett. 106 (2015), p. 162904.
[18] Y.X. Wang, W.L. Zhong, C.L. Wang, and P.L. Zhang, *First-principles study on the tendency to ferroelectricity of $CaTiO_3$*, Solid State Commun. 117 (2001), pp. 461–464.
[19] Y.X. Wang, M. Arai, T. Sasaki, and C.L. Wang, *First-principles study of the (001) surface of cubic $CaTiO_3$*, Phys. Rev. B 73 (2006), p. 035411.
[20] H. Lee, T. Mizoguchi, T. Yamamoto, and Y. Ikuhara, *First principles study on intrinsic vacancies in cubic and orthorhombic $CaTiO_3$*, Mater. Trans. 50 (2009), pp. 977–983.
[21] S. Saha, T.P. Sinha, and A. Mookerjee, *First principles study of electronic structure and optical properties of $CaTiO_3$*, Eur. Phys. J. B 18 (2000), pp. 207–214.
[22] Y.X. Wang, W.L. Zhong, C.L. Wang, and P.L. Zhang, *First principles study on the optical properties of cubic $CaTiO_3$*, Phys. Lett. A 291 (2001), pp. 338–342.
[23] M. Yamamoto, H. Ohta, and K. Koumoto, *Thermoelectric phase diagram in a $CaTiO_3$–$SrTiO_3$–$BaTiO_3$ system*, Appl. Phys. Lett. 90 (2007), p. 072101.
[24] T. Bak, T. Burg, J. Nowotny, and P.J. Blennerhassett, *Electrical conductivity and thermoelectric power of $CaTiO_3$ at n–p transition*, Adv. Appl. Ceram. 106 (2007), pp. 101–104.
[25] T. Bak, J. Nowotny, C.C. Sorrell, M.F. Zhou, and E.R. Vance, *Charge transport in $CaTiO_3$: II. Thermoelectric*, J. Mater. Sci. Mater. Electron. 15 (2004), pp. 645–650.
[26] P. Blaha, K. Schwarz, G.K.H. Madsen, D. Kvasnicka, and J. Luitz, *WIEN2K, An augmented plane wave + local orbitals program for calculating crystal properties*, Karlheinz Schwarz, Techn. Universitat Wien, Vienna, 2001.
[27] J.P. Perdew, A. Ruzsinszky, G.I. Csonka, O.A. Vydrov, G.E. Scuseria, L.A. Constantin, X. Zhou, and K. Burke, *Restoring the density-gradient expansion for exchange in solids and surfaces*, Phys. Rev. Lett. 100 (2008), p. 136406.

[28] A.D. Becke and E.R. Johnson, *A simple effective potential for exchange*, J. Chem. Phys. 124 (2006), p. 221101.
[29] F. Tran and P. Blaha, *Accurate band gaps of semiconductors and insulators with a semilocal exchange-correlation potential*, Phys. Rev. Lett. 102 (2009), p. 226401.
[30] S.M. Alay-e-Abbas, S. Nazir, and A. Shaukat, *Formation energies and electronic structure of intrinsic vacancy defects and oxygen vacancy clustering in BaZrO 3*, Phys. Chem. Chem. Phys. 41 (2016), pp. 521–530.
[31] S.M. Alay-e-Abbas, S. Nazir, N.A. Noor, N. Amin, and A. Shaukat, *Thermodynamic stability and vacancy defect formation energies in $SrHfO_3$*, J. Phys. Chem. C 118 (2014), pp. 19625–19634.
[32] G.K.H. Madsen and D.J. Singh, *BoltzTraP. A code for calculating band-structure dependent quantities*, Comput. Phys. Commun. 175 (2006), pp. 67–71.
[33] B. Luo, X. Wang, E. Tian, G. Li, and L. Li, *Electronic structure, optical and dielectric properties of $BaTiO_3$ /$CaTiO_3$/$SrTiO_3$ ferroelectric superlattices from first-principles calculations*, J. Mater. Chem. C 3 (2015), pp. 8625–8633.
[34] J. Long, L. Yang, and X. Wei, *Lattice, elastic properties and Debye temperatures of $ATiO_3$ (A=Ba, Ca, Pb, Sr) from first-principles*, J. Alloys Compd. 549 (2013), pp. 336–340.
[35] A.I. Lebedev, *Ab initio calculations of phonon spectra in $ATiO_3$ perovskite crystals (A = Ca, Sr, Ba, Ra, Cd, Zn, Mg, Ge, Sn, Pb)*, Phys. Solid State 51 (2009), pp. 362–372.
[36] M.F. Zhou, T. Bak, J. Nowotny, M. Rekas, C.C. Sorrell, and E.R. Vance, *Defect chemistry and semiconducting properties of calcium titanate*, J. Mater. Sci. Mater. Electron. 13 (2002), pp. 697–704.
[37] F. Wooten, *Optical Properties of Solids*, Academic, New York, 1972.
[38] D.R. Penn, *Wave-number-dependent dielectric function of semiconductors*, Phys. Rev. 128 (1962), pp. 2093–2097.
[39] K. Xiong, J. Robertson, and S.J. Clark, *Defect states in the high-dielectric-constant gate oxide LaAlO3*, Appl. Phys. Lett. 89 (2006), p. 022907.
[40] B.J. Kennedy, C.J. Howard, and B. Chakoumakos, *Phase transitions in perovskite at elevated temperatures – A powder neutron diffraction study*, J. Phys. Condens. Matter 11 (1999), pp. 1479–1488.
[41] G.J. Fischer, Z. Wang, and S.I. Karato, *Elasticity of $CaTiO_3$, $SrTiO_3$ and $BaTiO_3$ perovskites up to 3.0 Gpa: The effect of crystallographic structure*, Phys. Chem. Miner. 20 (1993), pp. 97–103.
[42] S. Saha, T.P. Sinha, and A. Mookerjee, *First principles study of electronic structure and optical properties of $CaTiO_3$*, Eur. Phys. J. B 18 (2000), pp. 207–214.
[43] K. Ueda, H. Yanagi, R Noshiro, and H. Hosono, *Vacuum ultraviolet reflectance and electron energy loss spectra of $CaTiO_3$*, J. Phys. Condens. Matter 10 (1998), p. 3669.